



Research article

Obtention of biochar-Fe/Ce using *Punica granatum* with high adsorption of ampicillin capacity



J.C. Gómez-Vilchis ^a, G. García-Rosales ^{a,*}, L.C. Longoria-Gándara ^b, E.O. Pérez-Gómez ^a, D.T. Castilleros ^c

^a TECNM/Instituto Tecnológico de Toluca/Departamento de Posgrado, Avenida Tecnológico 100 s/n. Colonia Agrícola, Bellavista, La Virgen, 52149 Metepec, Mexico

^b Division for Latin America/Department of Technical Cooperation International Atomic Energy Agency, Wagramer Strasse 5, P.O. Box 100, A-1400 Vienna, Austria

^c Instituto Nacional de Investigaciones Nucleares Departamento de Química, km. 36.5 carretera Mexico-Toluca s/n, La Marquesa, Ocoyoacac, Mexico

ARTICLE INFO

Keywords:
Adsorption
Ampicillin
Pomegranate
Iron
Cerium

ABSTRACT

This research presents the obtaining of a biochar (CB) from the use of pomegranate peel (*Punica granatum*) conditioned with iron and cerium nanoparticles (C-Fe/Ce), as well as its characterization by SEM (Scanning Electronic Microscopy), FTIR (Fourier Transform Infrared Spectrometry), TGA (Thermogravimetric analysis), EDS (Energy Dispersive Spectroscopy), XPS (X-Ray Photoelectron Spectroscopy) and evaluation of the adsorption capacity of ampicillin (AMP) in aqueous phase at 20, 30 and 40 °C. The maximum adsorption capacity for CB was 18.97 mg g⁻¹ and for C-Fe/Ce, 27.61 mg g⁻¹ at pH of 7, observing that with increasing temperature, the sorption capacity decreases in both materials, the experimental data was fitted to various mathematical models and the best fit was the pseudo-second order model for the kinetics, whilst for the adsorption isotherms the best fit was with the Langmuir model, indicating that the adsorption process is carried out in a monolayer on a homogeneous surface, through a chemisorption process. According to the thermodynamic parameters this process is carried out through an exothermic reaction. The results obtained indicate that both materials are suitable for the removal of AMP in the aqueous phase and that they can be reused up to 5 times.

1. Introduction

Micropollutants, also called ‘emerging pollutants’, consist of a large group of substances including pharmaceuticals, personal care products, steroid hormones, and agrochemicals [1]. These chemicals are related to anthropogenic activities and are normally transported mainly through aquatic environments and can have harmful effects on both aquatic organisms and humans through direct and indirect exposure [2]. However, pharmaceutical compounds are found in trace concentrations of ng L⁻¹ a µg L⁻¹, due to its wide use in veterinary medicine and humans, which then releases large amounts of pharmaceutical products into the environment [3].

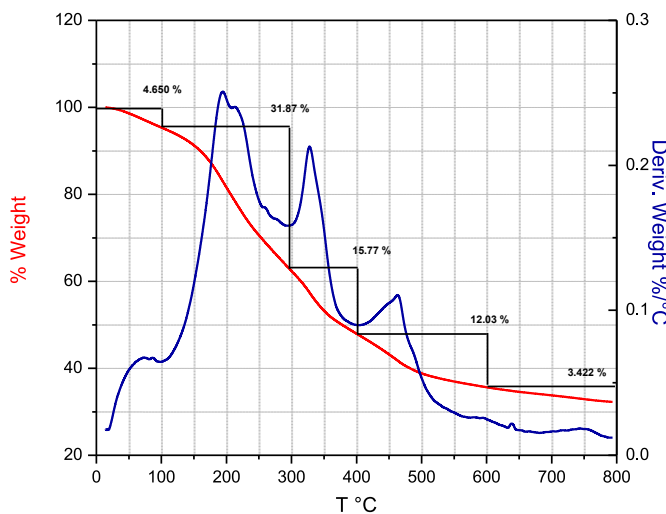
Ampicillin (AMP) is a semisynthetic β-lactam antibiotic that is taken by mouth and is most used in hospitals and veterinarians to kill infections caused by gram-positive and gram-negative bacteria [4]. This antibiotic contains in its structure a β-lactam ring that belongs to the group of penicillin's [5]. It is a non-biodegradable antibiotic that continues to remain in the water system for prolonged periods of time, thus causing its bioaccumulation that is why, at some point, these substances can reach

aquatic ecosystems [6], causing consequences, such as: the appearance of changes in the reproduction of fish due to the presence of hormones [7] and the inhibition of photosynthesis in algae by the presence of beta-blockers [8]. Due to high consumption and toxicity, AMP has been taken as a model drug for adsorption and controlled release studies [9].

Due to the structure that AMP has, it makes it difficult to remove it from the water, therefore, some processes have been studied for the exclusion of this pollutant, such as degradation [10] and oxidation [11]. However, the adsorption technique is widely used for the removal of various organic compounds from the water. Adsorption processes are considered relatively simple methods, effective in the removal of various pollutants in aqueous solution or industrial wastewater treatment [12]. For the removal of some organic pollutants, different adsorbent materials have been used for the elimination of organic pollutants in the aqueous phase, such as bentonite, chitosan [13], composites [14] and biochars [15]. This last material has been of great interest due to its high porosity and adsorption capacity [6], therefore, the objective of this research is to synthesize a biochar with and without Ce-Fe nanoparticles for the

* Corresponding author.

E-mail addresses: gegaromx@yahoo.com.mx, ggarciar@toluca.tecnm.mx (G. García-Rosales).

Figure 1. *Punica granatum* peel thermogram.

adsorption of AMP in the aqueous phase from the use of the peel from the *Punica granatum*.

2. Materials and methods

For this study the peel of *Punica granatum* was obtained in the Municipality of Tlaxcoapan, Hidalgo, Mexico. The reagents used were Fe (NO_3)₃·9H₂O (Sigma-Aldrich®, 98%) and (NH₄)₂·Ce (NO₃)₆ (Sigma-Aldrich®, 99.99%).

2.1. Preparation of CB and C-Fe/Ce

The *Punica granatum* peel was washed several times with distilled water at 120 °C for 30 min to remove impurities and dried in sunlight for 3 days and dried at 40 °C. It was ground and sieved to a size of 0.83 mm, thermal washes were carried out and subsequently dried at 35 °C for 48

Table 1. Specific surface area (Ae), volume and pore size.

| Material | Ae (m ² /g) | Pore Volume (cm ³ /g) | Pore size (nm) |
|----------|------------------------|----------------------------------|----------------|
| CB | 28.91 | 0.03 | 5.09 |
| C-Fe/Ce | 249.44 | 0.21 | 3.44 |

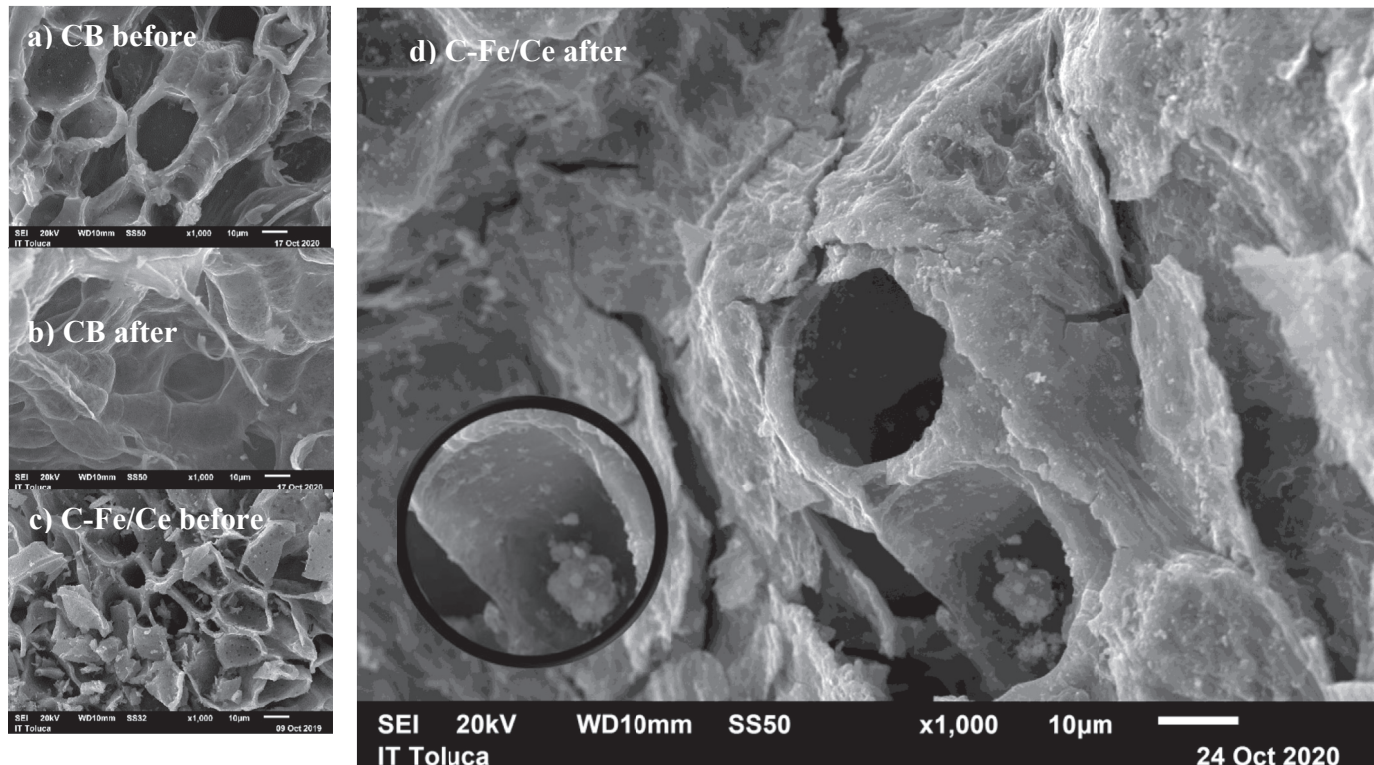


Figure 2. Micrograph of CB a) before sorption, b) After sorption; C-Fe/Ce c) before sorption, d) after sorption; e) CB pore size distribution after sorption, f) C-Fe/Ce pore size distribution and g) Fe/Ce particle size distribution.

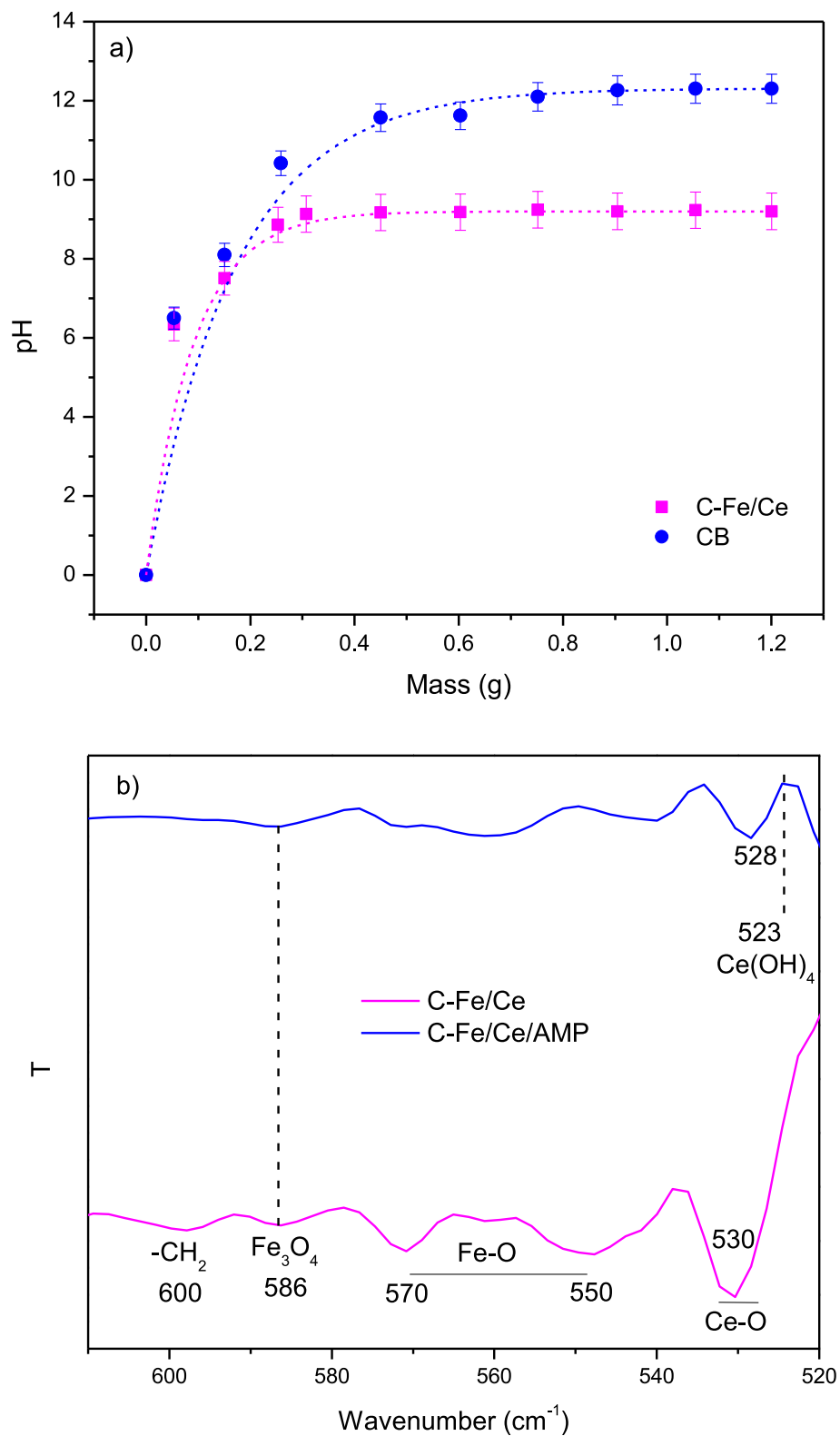


Figure 3. a) Isoelectric point, b) FTIR spectrum of Carbon-iron-cerium (C-Fe/Ce) before and after removal AMP.

h. *Punica granatum* treated with a NaOH 0.05 M solution for 20 min, subsequently, it was washed repeatedly with deionized water and dried at 30 °C. To define the optimal pyrolysis temperature, a thermogravimetric analysis was performed (TGA) of *Punica granatum*. Once the temperature was identified by means of TGA, the peel of *Punica granatum*

at 700 °C, thus obtaining biochar (CB), whilst the preparation of the composite consisted of mixing a solution of $\text{Fe}(\text{NO}_3)_3 \cdot 9\text{H}_2\text{O}$ and $(\text{NH}_4)_2\text{Ce}(\text{NO}_3)_6$ with 1 g of *Punica granatum* in a reactor that was sealed and placed in a shaking bath at 30 °C for 12 h, later it was pyrolyzed at the same temperature and given the name, C-Fe/Ce.

Table 2. Energy states (C-Fe/Ce).

| Element | Energy states | BE (eV) | FWHM | Relative area |
|---------|------------------|---------|------|---------------|
| C1s | C=O | 288.4 | 1.1 | 12.4 |
| | O-C-O | 287.5 | | 54.1 |
| | C-O | 286.7 | | 23.1 |
| | C=C | 284.8 | | 7.1 |
| | C-C | 284.3 | | 12.4 |
| O1s | OOC | 534.6 | 1.4 | 16.9 |
| | O-C | 533.2 | | 30.3 |
| | O-C-O | 532.4 | | 5.4 |
| | O=C | 531.7 | | 38.3 |
| | O-Metal | 530.3 | | 26.3 |
| Fe2p | Fe ³⁺ | 707.5 | 1.4 | 28.5 |
| | Fe ³⁺ | 709.1 | | 20.1 |
| | Fe ²⁺ | 710.5 | | 19.5 |
| | Fe ³⁺ | 712.1 | | 9.8 |
| Ce3d | v° | 881.7 | 2.4 | 14.1 |
| | V | 883.9 | | 9.8 |
| | v' | 885.8 | | 21.5 |
| | v'' | 887.8 | | 10.6 |
| | u° | 899.7 | | 9.7 |
| | U | 902.4 | | 11.6 |
| | u' | 904.71 | | 15.7 |
| | u'' | 907.12 | | 7.66 |

2.2. Characterization of materials

To determine the thermal degradation characteristics of the *Punica granatum* peel, an amount was analyzed in a TA Instruments-Waters SDT Q600 Calorimeter with a helium flow of 100 mL min⁻¹. Morphology and elemental distribution of the adsorbents (CB y C-Fe/Ce) were obtained with a microscope JEOL® JSM, model 5900 LV, which has a probe adapted for qualitative and quantitative analysis (EDS) brand OXFORD® model INCAx-Act 51-ADD0013 with a voltage of 20 kV. To determine the specific surface area of CB and C-Fe/Ce, the Brunauer-Emmett-Teller method was used in an N₂ atmosphere in the Belsorp® Max III equipment.

To identify the number of active sites (σ) in the adsorbents (CB and C-Fe/Ce), 30 mL of a 0.1 N NaClO₄ solution was put in contact with a known quantity of each material: CB and C-Fe/Ce, they were put in agitation for 24 h. After this time, the pH was measured and adjusted to ~ 2 with a 0.1 M HClO₄ solution. The resulting suspension was titrated with a 0.1 M NaOH solution until reaching pH ~ 12 . Throughout the process, the added mL and the pH variation was quantified with the Hanna Instruments® model HI8915 potentiometer, in the same way, a blank was titrated. With the data obtained from the titration and the value of the specific surface area of each material, the number of active sites per unit area was determined [16]. On the other hand, to know the isoelectric point of CB and C-Fe/Ce, different adsorbent masses were placed with 10 mL of deionized water at 30 °C in polypropylene tubes, the material was left for 24 h under constant stirring. Subsequently, the pH in each tube was measured using the HANNA® Instruments potentiometer. The analysis of the functional groups of the materials before and after the sorption process was carried out with an Infrared Spectrophotometer with Fourier Transform VARIAN® 640-IR, 16 scans were made to CB and C-Fe/Ce with a resolution of 4 cm⁻¹ in a range of 4000 to 500 cm⁻¹. The study of the energy states of the samples were carried out with an X-ray spectrophotometer Thermo Scientific K-Alpha X-Ray Photoelectron Spectrometer®, operating with an Al photoelectron source (K α). The equipment performed 10 scans per sample in a normal lens mode, aperture size 400 μ m, step size energy 0.030 eV.

2.3. Sorption studies

For the adsorption studies, a 100 mg L⁻¹ Ampicillin solution was prepared from a standard from the Sigma-Aldrich®. The AMP adsorption

kinetics were carried out in propylene tubes adding 1.5 mg of each adsorbent respectively with 5 mL of AMP at 5 mg L⁻¹ at different contact times: 10, 20 and 30 min, 1, 2, 3, 4, 5, 6, 8, 16 and 24 h, the tubes were shaken in a temperature-controlled bath at 20 °C, 30 °C and 40 °C. The data obtained was adjusted to the pseudo-first order, pseudo-second order and Elovich mathematical models and the AMP concentration in each supernatant was determined by UV-Vis at $\lambda = 255$ nm.

Whilst to evaluate the maximum adsorption capacity, adsorption isotherms were carried out by adding 1.5 mg of adsorbent with 5 mL of AMP at different concentrations in propylene tubes (4–12 mg L⁻¹). The tubes were shaken in a temperature-controlled bath at 20 °C, 30 °C and 40 °C for 24 h. The data obtained was adjusted to the mathematical models of Langmuir, Freundlich and Temkin. During the adsorption experiments, the pH was controlled at 7 \pm 0.2. The AMP concentration in each supernatant was determined by UV-Vis at $\lambda = 255$ nm.

However, the effect of the pH change in the adsorption process was studied and for this, 1.5 mg of adsorbent was placed in 5 mL of AMP solution at a concentration of 5 mg L⁻¹ in propylene tubes at different values in a pH range of 2–13 using NaOH and HNO₃ 0.1 M to adjust the pH. The tubes were shaken in a temperature-controlled bath at 20 °C for 24 h and the AMP concentration in each supernatant was determined by UV-Vis at $\lambda = 255$ nm.

The AMP removal percentages, as well as the sorption capacity q_e (mg g⁻¹) were calculated using Eqs. (1) and (2) respectively.

$$\% \text{ Removal} = \left[1 - \frac{C_e}{C_0} \right] \times 100 \quad (1)$$

$$q_e = \frac{(C_0 - C_e) V}{M} \quad (2)$$

Where: C_0 is the initial concentration and C_e is the equilibrium concentration mg L⁻¹; M (g) is the weight of the sorbent material and V (L) is the volume of the solution.

2.4. Activation energy studies

Once the kinetic data was collected and the rate constant was determined for the reaction at the three different temperatures (20, 30 and 40 °C) an Arrhenius plot was developed by plotting the Ln k against 1/T (K). The linearized form of the Arrhenius equation is given below in Eq. (3):

$$\ln k = \frac{Ea}{R} \left(\frac{1}{T} \right) + \ln A \quad (3)$$

Where k is the rate constant for the reaction at a given temperature, Ea is the activation energy for the process, R is the gas constant (8.314 kJ mol⁻¹), T is the temperature given in Kelvin, and A is the frequency factor for a given reaction.

2.5. Biochars reuse cycles

To evaluate the reuse of the biochar, 1 mg of each material obtained after the adsorption process was used with 5 mL of a solution at acid pH to desorb the AMP present in the solid, subsequently, the material was washed with deionized water and put in contact again with a solution of 5 mg g⁻¹ of AMP, this procedure was repeated 5 times. The remaining liquids were analyzed with UV-Vis at $\lambda = 255$ nm to determine the AMP concentration.

3. Results and discussion

3.1. Characterization

The TGA analysis of *Punica granatum* peel is presented in Figure 1, according to the graph the process can be divided into 4 stages: the first

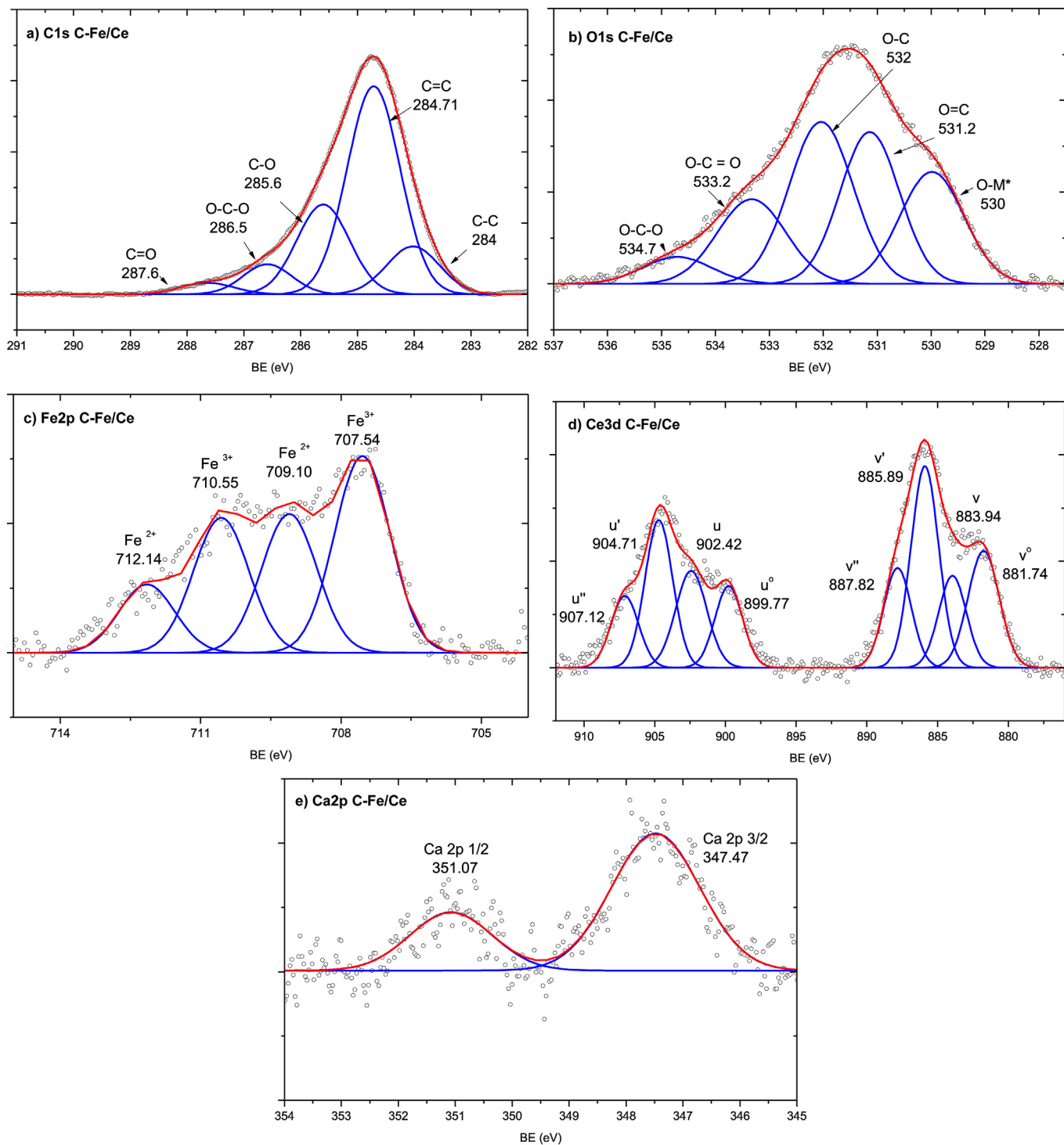


Figure 4. Deconvolution of a) C1s, b) O1s, c) Fe2p, d) Ce3d and e) Ca2p in C-Fe/Ce.

stage with a range from 15 °C to 100 °C, a decrease of 4.85% can be observed, which is common in some biosorbents [17, 18] and is associated with water loss [19]. The second stage (100–290 °C) shows two endothermic peaks, where there is a loss of 31.87 %, which is attributed to a decomposition of the organic material of hemicellulose [20]. The third stage (290–400 °C) occurs due to a continuous and simultaneous degradation process mainly due to the fact that there is a weight loss of 15.77 %, which can be attributed to the decomposition of cellulose [21]. Finally, the last stage known as slow degradation takes place between 400–600 °C with a weight loss of 12 % and is associated with the

degradation of lignin [22], which occurs in two phases, one from 400 to 600 °C and the other from 600 to 800 °C.

Likewise, the blue line represents the curve of the derivative of weight loss, where a band is shown at approximately 200 °C, and is attributed to the degradation of lignin or hemicellulose monomers, as well as the decomposition of pectin from *Punica granatum* peel [23] followed by a band at 325 °C that is due to the degradation of cellulose, which according to the literature occurs from 250 to 380 °C [24] also at 460 °C there is a band that refers to the complete decomposition of cellulose. Finally at 640 °C there is a smooth band that

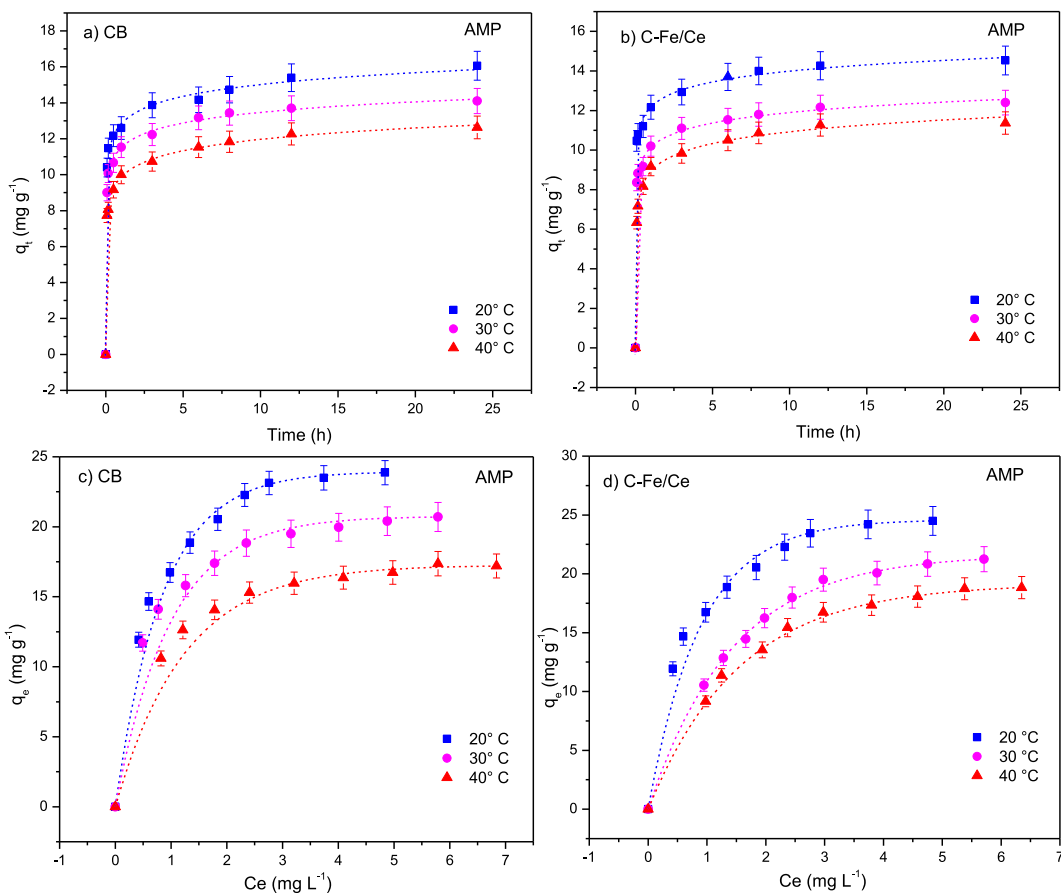


Figure 5. AMP adsorption kinetics with CB (a) to 20, 30 and 40 °C and with C-Fe/Ce (b). Isotherms in function of the initial concentration of AMP with CB a 20 °C, 30 °C y 40 °C (c) and C-Fe/Ce (d).

Table 3. Kinetic parameters of CB and C-Fe/Ce.

| Kinetic models Parameters | CB | | | C-Fe/Ce | | |
|------------------------------|--|--------|--------|---------|--------|-------|
| | 20 °C | 30 °C | 40 °C | 20 °C | 30 °C | 40 °C |
| Pseudo first order | $q_e \text{ (mg g}^{-1}\text{)}$ | 14.06 | 12.63 | 11.12 | 13.14 | 11.12 |
| | $K_L \text{ (h}^{-1}\text{)}$ | 13.78 | 12.61 | 10.83 | 16.05 | 13.75 |
| | R^2 | 0.917 | 0.919 | 0.890 | 0.920 | 0.906 |
| Pseudo second order | $q_e \text{ (mg g}^{-1}\text{)}$ | 14.52 | 13.07 | 11.57 | 12.67 | 11.51 |
| | $K_2 \text{ (g mg}^{-1} \text{ h}^{-1}\text{)}$ | 1.64 | 1.59 | 1.43 | -7.85 | 1.99 |
| | R^2 | 0.955 | 0.962 | 0.948 | 0.865 | 0.953 |
| Elovich | $\alpha \text{ (g mg}^{-1} \text{ h}^{-1}\text{)}$ | 7.11E5 | 2.99E5 | 4.58E4 | 4.26E6 | 4.4E5 |
| | $\beta \text{ (mg g}^{-1}\text{)}$ | 1.05 | 1.11 | 1.09 | 1.27 | 1.30 |
| | R^2 | 0.997 | 0.998 | 0.998 | 0.997 | 0.997 |

represents the decomposition of inorganic material such as metallic carbonates [19].

In Figure 2a), CB presents a set of hexagonal structures with thin and smooth walls covered by a delicate membrane, with an approximate diameter of 25 μm . EDS analysis indicates the presence of: C (78.35 %), O (15.90 %), Na (2.9 %), Ca (2.85 %) as the principal elements. After the process of sorption of AMP in CB (Figure 2b) the material presents some modifications in the structure, observing that the thin membrane that initially covers the hexagonal structures disappears and the hexagons undergo modifications presenting an average diameter of between 22 to 27 μm with about 4 μm thick, the hexagons form a honeycomb and well-defined pores are observed evenly distributed on their walls with an average diameter of 0.55 μm (Figure 2e) similar to those reported by Sahoo et al., [25] in bamboo stem. EDS analysis indicates the presence of

C (96.64 %), O (2.32 %), Na (0.48 %) and Ca (0.55 %). In general, some changes in the structure of CB are observed with the adsorption process, it is also distinguished that some parts of the material erode, as well as a slight increase in the atomic percentage of C, which can be attributed to the presence of the AMP in the material. Figure 2c) shows the C-Fe/Ce micrograph showing a rough surface with hexagonal cavities that form a honeycomb with some of the structures broken, which vary from 17 to 20 μm in diameter.

Defined pores are uniformly distributed in the cavities with an average diameter of 0.82 μm (Figure 2f). On the walls, the presence of Fe and Ce nanoparticles with an average diameter of 55 nm distributed on the surface of the material is observed spherical nanoparticles, in some areas the nanoparticles are also observed to form agglomerates (Figure 2g), general EDS analysis of the material indicates the presence of

Table 4. Adsorption isotherms.

| Mathematical Models | | CB | | | C-Fe/Ce | | |
|---------------------|-------------------------------|-----------|-----------|-----------|-----------|-----------|-----------|
| | | 20 °C | 30 °C | 40 °C | 20 °C | 30 °C | 40 °C |
| Langmuir | q_m (mg g ⁻¹) | 18.97 | 22.26 | 18.97 | 27.61 | 27.18 | 23.49 |
| | K_L (L mg ⁻¹) | 4.77 | 2.16 | 1.60 | 1.73 | 0.88 | 0.73 |
| | R^2 | 0.999 | 0.998 | 0.999 | 0.996 | 0.993 | 0.994 |
| | R_L | 0.13–0.04 | 0.10–0.03 | 0.13–0.04 | 0.12–0.04 | 0.25–0.10 | 0.25–0.10 |
| Freundlich | K_f (mg L ⁻¹) n | 12.15 | 14.90 | 12.15 | 16.92 | 12.27 | 1076 |
| | n | 4.91 | 4.77 | 4.91 | 3.65 | 2.86 | 2.98 |
| | R^2 | 0.987 | 0.988 | 0.987 | 0.984 | 0.974 | 0.975 |
| Temkin | q_m (mg g ⁻¹) | 792.85 | 667.15 | 846.94 | 453.20 | 409.03 | 499.89 |
| | K_T (mg L ⁻¹) | 48.88 | 59.60 | 48.88 | 24.20 | 6.54 | 7.00 |
| | R^2 | 0.992 | 0.994 | 0.992 | 0.993 | 0.987 | 0.988 |

Table 5. Comparison of the maximum sorption capacity (q_m) of AMP in CB and C-Fe/Ce with other materials.

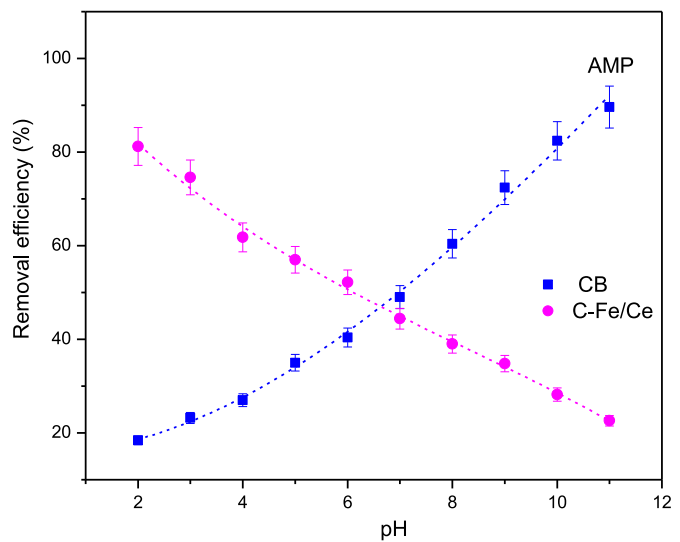
| Materials | q_m (mg/g) | Quantity (mg) | T (°C) | Concentration | Isotherm | References |
|------------------------------------|--------------|---------------|--------|---------------|----------------------|------------|
| Hidrogel | 245.09 | 100 | 45 | 10–100 mg/L | Langmuir | [9] |
| Activated carbón | 1.32 | 100 | 23 | 30–100 mg/L | Langmuir | [84] |
| | 1.87 | | | | | |
| Anionic surfactan | 2.30 | 250 | 25 | 1–100 mg/L | Langmuir | [76] |
| MCM-41 | 495 | 50 | 25 | 0.5–25 mg/mL | Langmuir | [85] |
| Montmorillonite NPs | 141.22 | 50 | - | 25 | Dubinin-Radushkevich | [86] |
| Polydopamine/zirconium (IV) iodate | 99.98 | 60 | 30 | 30–70 mg/L | Langmuir | [87] |
| | 102.90 | | 40 | | | |
| | 105.51 | | 50 | | | |
| CB 20 °C | 18.97 | 1.5 | 20 | 4–12 mg/L | Langmuir | This work |
| CB 30 °C | 22.26 | | 30 | | | |
| CB 40 °C | 18.97 | | 40 | | | |
| C-Fe/Ce 20 °C | 27.61 | 1.5 | 20 | 4–12 mg/L | Langmuir | |
| C-Fe/Ce 30 °C | 27.18 | | 30 | | | |
| C-Fe/Ce 40 °C | 23.49 | | 40 | | | |

Table 6. Thermodynamic parameters for sorption with CB and C-Fe/Ce.

| Material | Temperature (°C) | Thermodynamic parameters | | |
|----------|------------------|---------------------------|---------------------------|-----------------------------|
| | | ΔG° (kJ/mol) | ΔH° (kJ/mol) | ΔS° (J/mol °K) |
| CB | 20 | -1.16 | -33.12 | -0.10 |
| | 30 | -0.07 | | |
| | 40 | 1.02 | | |
| C-Fe/Ce | 20 | -3.63 | -41.88 | -0.13 |
| | 30 | -2.32 | | |
| | 40 | -1.02 | | |

CB (88.03 %), O (10.08 %), Fe (0.96 %) and Ce (0.93 %) as main elements. Figure 2d shows the micrograph of C-Fe/Ce after the sorption of AMP, where an eroded surface is observed, as well as the deformation of the hexagonal structures present before the adsorption process, however, the nanoparticles adhered to the walls of the structure. Likewise, it increases the size of the agglomerates of the nanoparticles on the surface of the material as a result from the adsorption process. The general EDS analysis shows the presence of: C (79.89 %), O (9.03 %), Na (1.14 %), Fe (3.61 %) and Ce (6.34 %).

The specific surface area (BET), volume and pore diameter of CB and C-Fe/Ce are shown in Table 1. It is observed that the specific area of C-Fe/Ce is greater than that of CB, this is due to the presence of nanoparticles in the material [26, 27]. Secondly, the difference of volume and pore size in both materials can be attributed to the fact that C-Fe/Ce has higher porosity than CB. The presence of pores can aid in the mass

**Figure 6.** AMP removal percentages with CB and C-Fe/Ce as a function of pH.

transfer so that AMP can easily reach active sites in the material. Also, when a porous material is conditioned with nanoparticles, and when these are formed, some are trapped in the walls of the cavities, resulting in a reduction in the size of the pores.

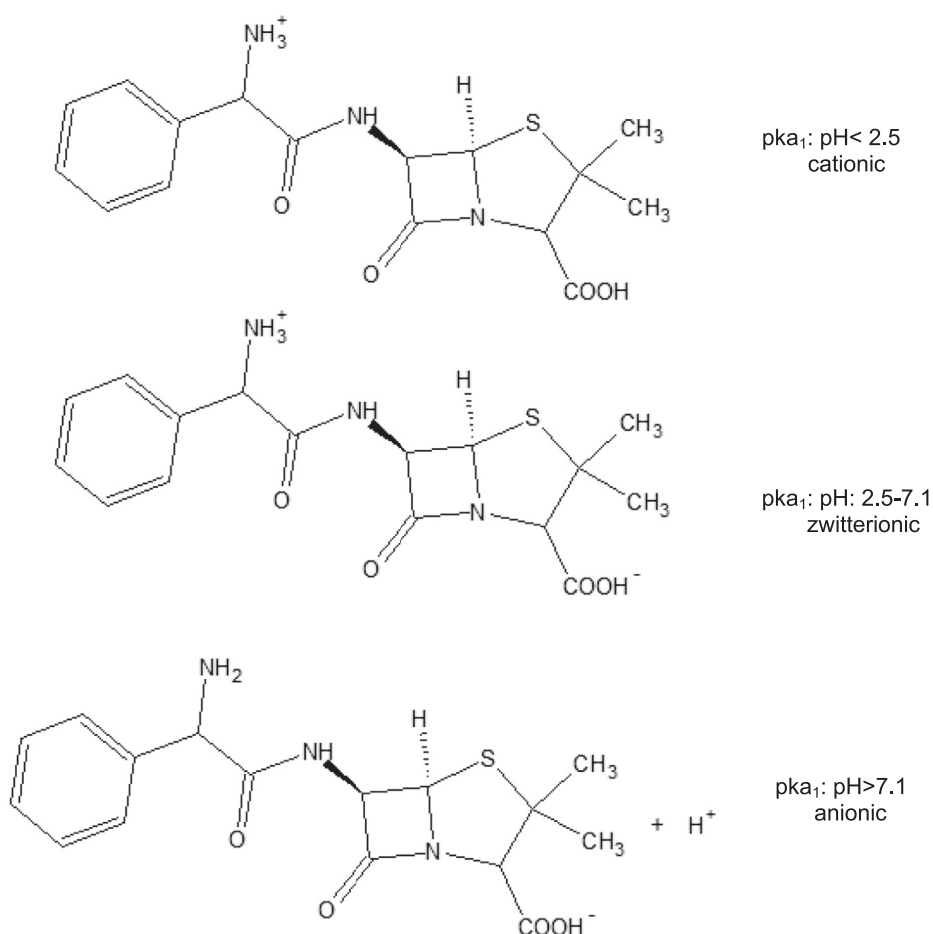


Figure 7. Effect of pH on ampicillin charge.

The surface sites' density in CB is 9 ± 1 sites nm^{-2} and 29 ± 1 sites nm^{-2} for C-Fe/Ce; between the two materials there is a difference of 20 ± 1 sites nm^{-2} , so the number of active sites of C-Fe/Ce is 3 times greater than that of CB, this result indicates that the presence of nanoparticles in the carbonaceous matrix increases the density of active sites and therefore its adsorption capacity is expected to be higher [28].

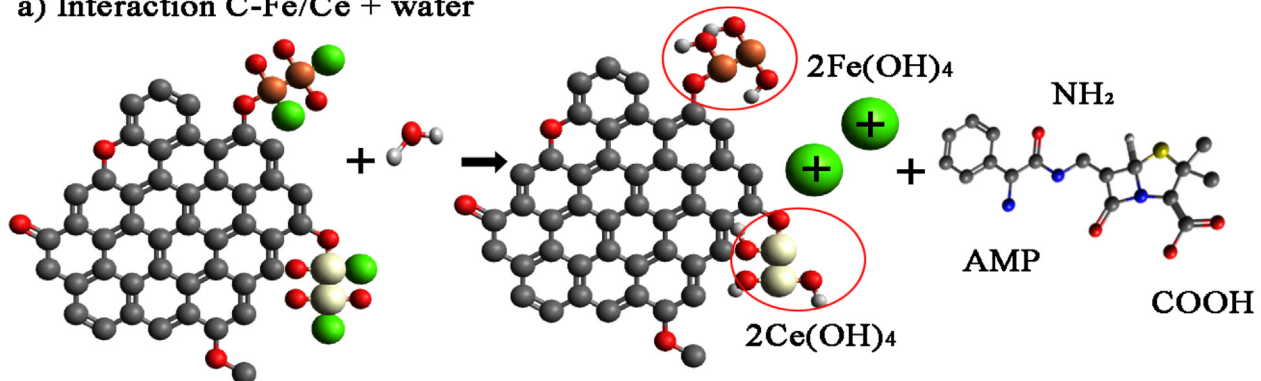
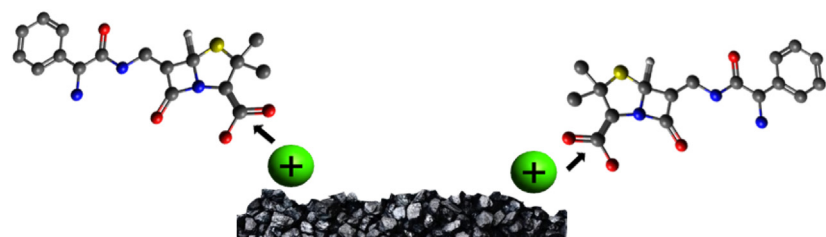
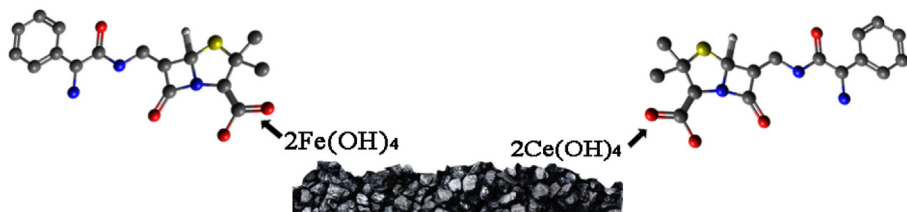
The results of the isoelectric point (pH_{zpc}) shown in Figure 3a), indicate the pH where the charges of each material are in equilibrium due to the transfer of ions [H^+] and [OH^-], for CB was observed the pH_{zpc} at $pH = 12 \pm 0.03$ whilst for C-Fe/Ce was of $pH = 9 \pm 0.03$. The results obtained are favourable for the adsorption of AMP. In the literature, values close to 12 have been reported for carbonaceous materials whilst for those conditioned with nanoparticles the values range between 9 and 10 [29].

FTIR spectra of C-Fe/Ce before and after sorption are presented in Figure 3b) where to 600 cm^{-1} is present the aromatic vibration $-\text{CH}_2$, and is observed that after adsorption process disappears; the bands in the range of $520\text{--}590 \text{ cm}^{-1}$ are attributed to the presence of O-Metal [30], for the magnetite Fe_3O_4 (586 cm^{-1}) are observed the groups Fe-O ($570\text{--}550 \text{ cm}^{-1}$) [31] and Ce-O (530 cm^{-1}). However, after the sorption of AMP, the vibrations from $570\text{--}550 \text{ cm}^{-1}$ decrease in intensity, which suggests that an interaction between Fe-O and the AMP molecule, because Fe-O in an acid medium can be form cations that bind with the AMP anion's groups [32, 33, 34, 35, 36, 37]. According to the results obtained at the isoelectric point in a pH range of 1–9, the surface of the material is positively charged, favoring the attraction of anions of the AMP through electrostatic interaction. Whilst the Ce-O vibration in 530 cm^{-1} after the sorption of AMP presents a slight displacement in 528 cm^{-1}

cm^{-1} due to the formation of $\text{Ce}(\text{OH})_4$. In general, the FTIR spectra obtained for C-Fe/Ce showed that after adsorption, the intensities of the peaks decreased, and some shifts occurred because of the interaction of AMP with the surface of the material [38, 39].

According to the results obtained in XPS, Table 2 shows the energy states of C-Fe/Ce. In Figure 4a) the changes of energy states of C-Fe/Ce in C1s are presented, the energy of the peaks at 284 and 284.71 eV correspond to C-C and C=C belonging to the carbonyl group [40], the peaks at 285.6, 286.5 and 287.6 eV correspond to the C-O, O-C-O and C=O groups respectively in the bonds present in the carboxyl or ester group, which are common in some composites obtained from organic residues [41, 42, 43]. The deconvolution of O1s is shown in Figure 4b), where a peak is observed at 530 eV which corresponds to metallic oxides, such as O-Fe and O-Ce present in the material [44, 45], which are common in some carbon-metal composites [46]. Likewise, there is the participation of O=C, O-C and O-C=O in the peaks 531.2, 532 and 533.2 eV respectively, which represent oxygen atoms in esters and hydroxyl present in the material [47, 48, 49], in 534.7 eV presents itself O-C- corresponds to the carbonate group [50].

On the other hand, in Figure 4c) the energy states for Fe2p in C-Fe/Ce, can be found Fe^{2+} to 709.14 and 712.14 eV also it shows the presence of Fe^{3+} in 710.55 eV [51, 52]. In general, the countant of Fe^{2+} must be reduced due to its participation in the reaction with carbon or oxygen, however, the increase in the proportion of Fe^{2+} indicates that the presence in C-Fe/Ce can promote the reduction of Fe^{3+} to Fe^{2+} by obtaining electrons from the same material ($\text{Fe}^0 - 2\text{e}^- \rightarrow \text{Fe}^{2+}, 2\text{Fe}^{3+} + \text{Fe}^0 \rightarrow 3\text{Fe}^{2+}$) [53]. In the spectrum of Ce3d there are two divided doublets that represent the components of Ce3d 5/2

a) Interaction C-Fe/Ce + water**b) Cationic attraction****c) Anionic attraction****d) Hydrogen bonds****Figure 8.** Mechanism of AMP adsorption on C-Fe/Ce.

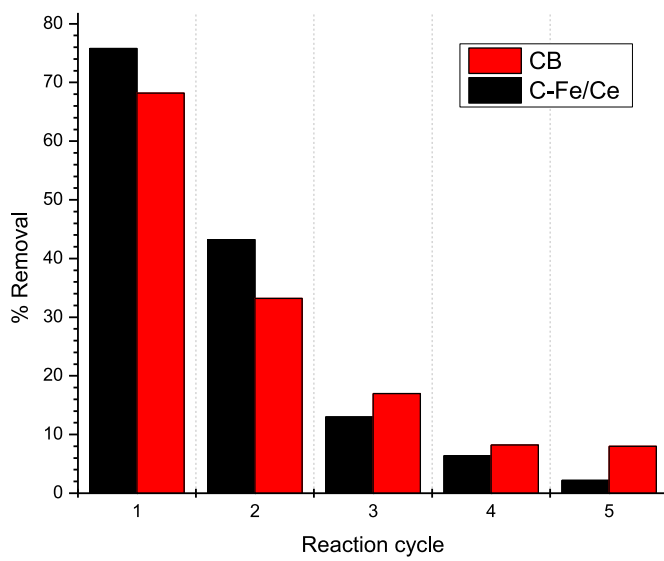


Figure 9. AMP reuse cycle's on CB and C-Fe/Ce.

(represented as v) and Ce3d 3/2 (represented as u). As shown in Figure 4d) the peaks are at 883.94, 899.77, 902.42 and 907.12 eV were named v, u⁰, u and u'' respectively and are attributed to Ce⁴⁺, whilst the four remaining peaks located at 881.74, 885.89, 887.82 and 904.71 eV named v⁰, v', v'' and u' represent the Ce³⁺ [54, 55], which are present in some composites C-Ce [56, 57].

According to the literature the Ce³⁺ can oxide as Ce⁴⁺ in contact with air at room temperature. However, in this work, the formation of cerium nanoparticles were accompanied by the carbonization of the *Punica granatum* peel under an inert atmosphere during the pyrolysis process where a complete reduction occurred that inhibited the oxidation of Ce³⁺. Therefore, the coexistence of the 4⁺ and 3⁺ states of Ce is indicative of a synergistic interaction between the redox pairs Fe³⁺/Fe²⁺ and Ce⁴⁺/Ce³⁺, at the vacant oxygen sites in the material through a redox equilibrium [58, 59]. The deconvolution of Ca2p is shown in Figure 4e), where two energies are presented at 347.47 and 351.07 eV, which are associated with Ca 2p3/2 and Ca 2p1/2, respectively corresponding to CaCO₃ [60, 61].

3.2. Adsorption kinetics

The results obtained in the sorption kinetics of AMP as a function of time are shown in Figure 5a–b). Where it can be observed that for CB at temperatures of 20 °C, 30 °C and 40 °C the kinetic equilibrium begins at 3 h of contact, reaching equilibrium after 12 h with 14.26, 12.16 and 11.26 mg/g respectively. Similarly, it can be seen that the kinetic balance of C-Fe/Ce corresponds to the times mentioned above, with 15.14, 13.70 and 12.26 mg/g, for temperatures of 20 °C, 30 °C and 40 °C, respectively. With the above, it is observed that the presence of Fe/Ce nanoparticles in the biochar favours the kinetic balance of the sorption of AMP, these results are related to the difference that exists between the density of active sites of both materials (section 3.1).

The experimental data of the adsorption kinetics of AMP with CB and C-Fe/Ce at different temperatures were adjusted to the pseudo-first order (Eq. (4)) [62], pseudo-second (Eq. (5)) [63] and Elovich (Eq. (6)) [64] kinetic models (Figure 5). Finding that the best fit was to the Elovich model (Eq. (3)) with correlation coefficients of 0.997–0.998, indicating that the adsorption process presents feasibility because the α values are greater than the β values (Table 3), which represents that the adsorption rate is greater than the desorption [65].

The pseudo-first-order model or Lagergren expression (Eq. (4)) consists of an equation based on a surface reaction generally expressed as:

$$q_t = q_e (1 - e^{(-k_L t)}) \quad (4)$$

k_L is Lagergren adsorption rate constant ($\text{g mg}^{-1}\text{min}^{-1}$), q_e is the concentration of the adsorbate in the adsorbent at equilibrium (mg g^{-1}) and q_t is the concentration of the adsorbate in the adsorbent at a given time (mg g^{-1}).

The pseudo-second-order model (Eq. (5)) relates the solute to the active sites on the surface of the sorbent, assuming that the sorption capacity is proportional to the number of active sites occupied in the sorbent.

$$q_t = \frac{k_2 q_e^2 t}{1 + k_2 q_e t} \quad (5)$$

Here, the k_2 ($\text{g mg}^{-1}\cdot\text{min}$) is the rate constant of the pseudo-second order model.

The Elovich model (Eq. (6)) is useful to predict the mass and surface diffusion, activation, and deactivation energy of an adsorbate-adsorbent system.

$$q_t = \frac{1}{\beta} \ln t + \frac{1}{\beta} \ln \alpha \beta \quad (6)$$

Where: q_t is the amount of adsorbate on the adsorbent surface at time t (mg g^{-1}). α ($\text{g mg}^{-1}\text{h}^{-1}$) and β (mg g^{-1}) are the Elovich coefficients that represent the initial adsorption rate and the desorption coefficient.

3.3. Adsorption isotherms

The adsorption results as a function of the concentration were adjusted to the mathematical models of Langmuir (Eq. (7)), Freundlich and Temkin to evaluate the adsorption capacity of the materials (Figure 5c–d). According to the results (Table 4), the experimental data has a better fit to the Langmuir mathematical model with a correlation coefficient very close to 1 for CB and for C-Fe/Ce with q_m values of 18.97, 22.26, 18.97 mg g⁻¹ for CB at 20 °C, 30 °C and 40 °C, respectively. Whilst, for C-Fe/Ce they were 27.61, 27.18 and 23.49 mg g⁻¹ at the same temperatures mentioned above, therefore, the adsorption of AMP in both materials is carried out in a monolayer on a homogeneous surface [66, 67]. It should be noted that the presence of nanoparticles on the surface of the material [68] leads to an increase in the adsorption capacity of AMP. Langmuir's model is expressed in Eq. (7):

$$\frac{C_e}{q_e} = \frac{1}{K_L q_m} + \frac{1}{q_m} \quad (7)$$

Where: q_e is the adsorption capacity at equilibrium (mg g^{-1}), C_e is the concentration of AMP at equilibrium (mg/L), q_m is the maximum adsorption capacity (mg g^{-1}), K_L is the Langmuir constant, related to adsorption energy.

The principle characteristics of the Langmuir isotherm is represented by the dimensionless constant $RL = 1/(1 + K_L C_0)$. When $RL > 1$ presents an unfavourable adsorption, $RL = 1$ is linear and $RL < 1$ is favourable and $RL = 0$ presents an irreversible adsorption [69]. In this investigation, the RL values are between 0 and 1 (Table 4). This shows that the AMP molecule has a strong affinity for CB and C-Fe/Ce. Whereas the fit of the Freundlich adsorption model can be discussed according to the value of n. Where $n < 1$ presents a weak adsorption, n between 1 and 2 moderate adsorption and n between 2 and 10 good adsorption [70]. Considering the values of n obtained, there is a good adsorption of AMP in CB and C-Fe/Ce. On the other hand, the data obtained in the Temkin isotherm of b and KT represent the interaction of the materials with the pollutant [71]. With the data obtained from the sorption kinetics of AMP, the activation energy was calculated, finding that for CB it was 1507 kJ mol⁻¹, while for C-Fe/Ce it was 3168 kJ mol⁻¹, which suggests that a chemisorption process occurs during adsorption process [72], because below 40 kJ mol⁻¹ it obeys a process of physisorption and above that

energy the process of chemisorption takes place, since this process requires more energy [73].

Table 5 shows the comparison of the maximum adsorption capacity (q_m) of AMP for CB and C-Fe/Ce at different temperatures with those obtained in other investigations. It should be mentioned that, although the experimental conditions used are different, it is valid to compare the values of q_m , since the sorption capacity is a criterion that provides an idea about the performance of CB and C-Fe/Ce with respect to other materials. Some researchers have reported higher sorption capacities than CB and C-Fe/Ce, however, most use a greater amount of adsorbent material to perform sorption experiments, therefore, the advantage that CB and C-Fe/Ce with respect to the other materials is that the amount of mass used is 1.5 mg.

3.4. Thermodynamic parameters

To investigate the effect of temperature on the adsorption of AMP in CB and C-Fe/Ce, three different adsorption temperatures were used (20 °C, 30 °C and 40 °C). As seen in **Table 6**, the thermodynamic parameters show that as the temperature increases, the interaction between the materials and the AMP molecule decreases. Using the following Eqs. (8) and (9), ΔH° , ΔS° and ΔG° were calculated.

$$\Delta G^\circ = \Delta H^\circ - T\Delta S^\circ \quad (8)$$

$$\ln k = -\frac{\Delta^\circ H}{R} * \frac{1}{T^\circ} + \frac{\Delta^\circ S}{R} \quad (9)$$

For both materials the values of ΔH° and ΔS° are negative, which indicates an increase in the randomness in the liquid-solid interface (adsorbent) during the adsorption process and an exothermic nature of the sorption process, in addition there is a strong interaction between the sorbent and the chemical species of the compounds [74]. The increase in temperature in the system decreases the binding potential at equilibrium, therefore, the adsorption capacity also decreases [75], both for C-Fe/Ce and for CB.

On the other hand, negative values of ΔG° suggest a decrease in Gibbs free energy, showing the viability of an adsorption process through electrostatic interaction between sorbate and sorbent [76]. However, Munagapati & Kim [77] and Bansalet al., [78] reported that the decrease in the sorption of organic compounds in some materials is due to the increase in the sorption temperature, which leads to an exothermic process occurring. Therefore, the decrease can be attributed to the weakening of the van der Waals attraction forces between AMP molecules and C-Fe/Ce surfaces [79], whilst in CB they can coexist at 40 °C, due to the observation in ΔG° , which suggests an endothermic process. The results obtained for ΔH° are below -100 kJ/mol, indicating that the interaction between AMP and the surface of the material is carried out through a physisorption process. The ΔG° trends indicate that as the temperature in the system increases, these values increase, indicating that the adsorbed quantity decreases which makes the system more available for the adsorption process.

3.5. Effect of pH and the sorption mechanism of AMP

The isotherm of AMP adsorption with respect to pH is presented in **Figure 6**. In which can be seen that by increasing the pH in CB, the percentage of AMP adsorption increases, with a maximum of 89.6%. This behaviour is due to the pHzc of the material being 12, and when pH value is less than 12 the surface charge of the sample is positive, which attracts the anionic structure of the AMP. For C-Fe/Ce, the removal percentage of AMP decreases when the pH in the solution increases, it decreases from 81.2% to 22.6%, this might be because the pHzc of the material being 9, which suggests that at lower pH the C-Fe/Ce presents higher removal performance. This is because the main sorption

mechanism is carried out by chemisorption, which is related to the adjustments of the kinetic and isothermal models of adsorption.

pH is an important factor that affects the adsorption behaviour. The pH of the solution strongly affects the structure of the AMP. In **Figure 7** the effect of pH on the charge of AMP is shown, where it can be observed that at pH less than 2.5 it presents a cationic structure, however, between 2.5 and 7 it shows a dipolar structure; but at pH above 7 an anionic structure is the predominant species.

The mechanisms involved in the removal of AMP was obtained using Avogadro Vision 1.2.0. software and is presented in **Figure 8**. In which can be seen that in C-Fe/Ce, the structure of CB is conditioned with Fe and Ce ions at the time of the synthesis of the material. In **Figure 8a**) the interaction of C-Fe/Ce with H₂O is shown, which forms hydroxylated species on the surface, for metal with Ca [80, 81], due to the oxidation states of Fe and Ce in the material, which are related in the XPS study.

In **Figure 8b**), it is shown that the predominant charges are positive, because the pHzc is 9 ± 0.1 , where Ca²⁺ interacts with the amino group (NH₂) present in the structure of AMP [82], which is known as cationic attraction. In **Figure 8c**) an anionic attraction is presented, where at pH greater than 9 the surface is negatively charged, and the predominant iron and cerium states are Fe³⁺ and Ce⁴⁺, which have greater affinity for the OH⁻ bonds present in the AMP molecule. Whilst in **Figure 8d**) it can be seen that the OH⁻ on the surface of the material could act as a donor of H⁺ and form hydrogen bonds with the oxygen atom present in the AMP molecule [83].

3.6. Reuse cycles

To determine the reuse capacity of the material, adsorption tests were carried out using a 5 mg L⁻¹ AMP solution. **Figure 9** shows the adsorption percentages at 20 °C, ≤ 65 % and ≤ 75 % for CB and C-Fe/Ce, were obtained, respectively during the first reuse cycle and subsequently the adsorption capacity in both materials decreases. As for the second and third cycles, it remains at 33.2 % and 17 % and finally, for the fourth and fifth cycles, it decreases to 8.2 % and 8 %. On the other hand, for C-Fe/Ce the adsorption of the material decreases more compared to CB because in the last cycle there is a removal of 2.2 %.

4. Conclusions

In this work C-Fe/Ce and CB were synthesized using *Punica granatum* husk, where according to the ATG, the optimum pyrolysis temperature was 700 °C. Likewise, the nature of the materials obtained were studied using different characterization techniques, which confirmed the presence of iron and cerium nanoparticles with average sizes of 55 nm in the biochar. Both materials have a good adsorption capacity, being the best C-Fe/Ce due to the nanoparticles present in the biocarbon that help increase the sorption capacity of AMP. When using both materials, the highest efficiency was obtained at 20 °C, at a pH of 7 ± 0.1 with a contact time of 24 h, additionally both materials can be reused 5 times. The mathematical models to which the isotherms were best adjusted were Elovich and Langmuir isotherm, indicating that the adsorption process is carried out through a chemisorption process. According to the results obtained by FTIR and XPS, three different adsorption mechanisms are proposed: cationic and anionic interaction and hydrogen bonding. Finally, the thermodynamic parameters indicate that the adsorption process is exothermic because with increasing the temperature, the adsorption capacity decreases.

Declarations

Author contribution statement

J. C. Gómez-Vilchis: Performed the experiments; Analyzed and interpreted the data; Wrote the paper.

G. García-Rosales & L.C. Longoria-Gándara: Conceived and designed the experiments; Analyzed and interpreted the data; Contributed reagents, materials, analysis tools or data; Wrote the paper.

E. O. Pérez-Gómez: Analyzed and interpreted the data; Wrote the paper.

D. Tenorio-Castilleros: Analyzed and interpreted the data; Wrote the paper.

Funding statement

This work was partially supported by TECNM.

Data availability statement

The authors do not have permission to share data.

Declaration of interests statement

The authors declare no conflict of interest.

Additional information

No additional information is available for this paper.

Acknowledgements

The authors gratefully acknowledge to TECNM for the partial financial support of this work. J.C. Gómez-Vilchis and E.O. Pérez-Gómez acknowledges CONACYT for the M.S. fellowships received in support of this work.

References

- [1] M.J. Ahmed, Adsorption of quinolone, tetracycline, and penicillin antibiotics from aqueous solution using activated carbons: Review, Environ. Toxicol. Pharmacol. 50 (2017) 1–10.
- [2] L. Yang, Y. Zhou, B. Shi, J. Meng, B. He, H. Yang, S.J. Yoon, T. Kim, B.-O. Kwon, J.S. Khim, T. Wang, Anthropogenic impacts on the contamination of pharmaceuticals and personal care products (PPCPs) in the coastal environments of the yellow and Bohai seas, Environ. Int. 135 (2020) 105306.
- [3] C. Miège, J.M. Choubert, L. Ribeiro, M. Eusebe, M. Coquery, Fate of pharmaceuticals and personal care products in wastewater treatment plants—conception of a database and first results, Environ. Pollut. 157 (5) (2009) 1721–1726.
- [4] B. Thakuria, The beta lactam antibiotics as an empirical therapy in a developing country: an update on their current status and recommendations to counter the resistance against them, J. Clin. Diagn. Res. (2013).
- [5] D. Nathwani, M.J. Wood, Penicillins, Drugs 45 (6) (1993) 866–894.
- [6] H.R. Pouretedal, N. Sadegh, Effective removal of amoxicillin, cephalaxin, tetracycline and penicillin G from aqueous solutions using activated carbon nanoparticles prepared from vine wood, J. Water Proc. Eng. 1 (2014) 64–73.
- [7] J.B. Fursdon, J.M. Martin, M.G. Bertram, T.K. Lehtonen, B.B.M. Wong, The pharmaceutical pollutant fluoxetine alters reproductive behaviour in a fish independent of predation risk, Sci. Total Environ. 650 (Pt 1) (2019) 642–652.
- [8] B.I. Escher, N. Bramaz, M. Richter, J. Lienert, Comparative ecotoxicological hazard assessment of beta-blockers and their human metabolites using a mode-of-action-based test battery and a QSAR approach, Environ. Sci. Technol. 40 (23) (2006) 7402–7408.
- [9] B. Thakur, G. Sharma, A. Kumar, S. Sharma, M. Naushad, J. Iqbal, F.J. Stadler, Designing of bentonite based nanocomposite hydrogel for the adsorptive removal and controlled release of ampicillin, J. Mol. Liq. 319 (2020) 114166.
- [10] R.M. Balakrishnan, I. Ilango, G. Gamana, X.-T. Bui, A. Pugazhendhi, Cobalt ferrite nanoparticles and peroxymonosulfate system for the removal of ampicillin from aqueous solution, J. Water Proc. Eng. 40 (2021) 101823.
- [11] L. Ioannou-Ttofa, S. Raj, H. Prakash, D. Fatta-Kassinos, Solar photo-Fenton oxidation for the removal of ampicillin, total cultivable and resistant *E. coli* and ecotoxicity from secondary-treated wastewater effluents, Chem. Eng. J. 355 (2019) 91–102.
- [12] E. Worch, Adsorption Technology in Water Treatment: Fundamentals, Processes, and Modeling, De Gruyter, Berlin, Boston, 2012.
- [13] P. Sirajudheen, P. Karthikeyan, S. Vigneshwaran, M. Nikitha, C.A.A. Hassan, S. Meenakshi, Ce(III) networked chitosan/β-cyclodextrin beads for the selective removal of toxic dye molecules: adsorption performance and mechanism, Carbohydr. Polym. Technol. Appl. 1 (2020) 100018.
- [14] F. Mahmoudi, M.M. Amini, M. Sillanpää, Hydrothermal synthesis of novel MIL-100(Fe)@SBA-15 composite material with high adsorption efficiency towards dye pollutants for wastewater remediation, J. Taiwan Inst. Chem. Eng. 116 (2020) 303–313.
- [15] J. Liu, X. Yang, H. Liu, W. Cheng, Y. Bao, Modification of calcium-rich biochar by loading Si/Mn binary oxide after NaOH activation and its adsorption mechanisms for removal of Cu(II) from aqueous solution, Colloids Surf. A Physicochem. Eng. Asp. 601 (2020) 124960.
- [16] L. Bell, A. Posner, J. Quirk, The point of zero charge of hydroxyapatite and fluorapatite in aqueous solutions, J. Colloid Interface Sci. 42 (2) (1973) 250–261.
- [17] M. Ahmad, M. Ahmad, A.R.A. Usman, A.S. Al-Faraj, A. Abduljabbar, Y.S. Ok, M.I. Al-Wabel, Date palm waste-derived biochar composites with silica and zeolite: synthesis, characterization and implication for carbon stability and recalcitrant potential, Environ. Geochem. Health (2017).
- [18] M.A. Hassaan, A. El Nemr, M.R. Elkatory, S. Ragab, M.A. El-Nemr, A. Pantaleo, Synthesis, characterization, and synergistic effects of modified biochar in combination with α -Fe₂O₃ NPs on biogas production from red algae pterocladia capillacea, Sustainability 13 (2021) 9275.
- [19] W. Saadi, S. Rodríguez-Sánchez, B. Ruiz, S. Souissi-Najar, A. Ouederni, E. Fuente, Pyrolysis technologies for pomegranate (*Punica granatum L.*) peel wastes. Prospects in the bioenergy sector, Renew. Energy 136 (2019) 373–382.
- [20] S. Ben-Ali, I. Jaouali, S. Souissi-Najar, A. Ouederni, Characterization and adsorption capacity of raw pomegranate peel biosorbent for copper removal, J. Clean. Prod. 142 (2017) 3809–3821.
- [21] M. Hussain, L. Dendena Tufa, S. Yusup, H. Zabiri, Thermochemical behavior and characterization of palm kernel shell via TGA/DTG technique, Mater. Today Proc. 16 (2019) 1901–1908.
- [22] Z. Ma, D. Chen, J. Gu, B. Bao, Q. Zhang, Determination of pyrolysis characteristics and kinetics of palm kernel shell using TGA-FTIR and model-free integral methods, Energy Convers. Manag. 89 (2015) 251–259.
- [23] X. Yang, T. Nisar, Y. Hou, X. Gou, L. Sun, Y. Guo, Pomegranate peel pectin can be used as an effective emulsifier, Food Hydrocolloids 85 (2018) 30–38.
- [24] K. Slopiecka, P. Bartocci, F. Fantozzi, Thermogravimetric analysis and kinetic study of poplar wood pyrolysis, Appl. Energy 97 (2012) 491–497.
- [25] S.S. Sahoo, V.K. Vijay, R. Chandra, H. Kumar, Production and characterization of biochar produced from slow pyrolysis of pigeon pea stalk and bamboo, Clean Technol. Environ. Policy 3 (2021) 100101.
- [26] A. Choudhury, S. Lansing, Adsorption of hydrogen sulfide in biogas using a novel iron-impregnated biochar scrubbing system, J. Environ. Chem. Eng. 9 (1) (2021) 104837.
- [27] M.A. Ciciliati, M.F. Silva, D.M. Fernandes, M.A.C. de Melo, A.A.W. Hechenleitner, E.A.G. Pineda, Fe-doped ZnO nanoparticles: synthesis by a modified sol-gel method and characterization, Mater. Lett. 159 (2015) 84–86.
- [28] A. Opalinska, I. Malka, W. Dzwolak, T. Chudoba, A. Presz, W. Lojkowski, Size-dependent density of zirconia nanoparticles, Beilstein J. Nanotechnol. 6 (2015) 27–35.
- [29] B. D'Cruz, M. Madkour, M.O. Amin, E. Al-Hetlani, Efficient and recoverable magnetic AC-Fe₃O₄ nanocomposite for rapid removal of promazine from wastewater, Mater. Chem. Phys. 240 (2020) 122109.
- [30] N. Priyadarshni, P. Nath, Nagahnumaiah, N. Chanda, Sustainable removal of arsenate, arsenite and bacterial contamination from water using biochar stabilized iron and copper oxide nanoparticles and associated mechanism of the remediation process, J. Water Proc. Eng. 37 (2020) 101495.
- [31] D. Bao, Z. Li, R. Tang, C. Wan, C. Zhang, X. Tan, X. Liu, Metal-modified sludge-based biochar enhance catalytic capacity: characteristics and mechanism, J. Environ. Manag. 284 (2021) 112113.
- [32] N. Zafar, B. Uzair, M. Niaz, F. Menaa, G. Samin, B.A. Khan, H. Iqbal, B. Menaa, Green synthesis of ciprofloxacin-loaded cerium oxide/chitosan nanocarrier and its activity against MRSA-induced mastitis, J. Pharmacol. Sci. 110 (10) (2021) 3471–3483.
- [33] J. Shin, Y.-G. Lee, J. Kwak, S. Kim, S.-H. Lee, Y. Park, S.-D. Lee, K. Chon, Adsorption of radioactive strontium by pristine and magnetic biochars derived from spent coffee grounds, J. Environ. Chem. Eng. 9 (2021) 105119.
- [34] H.T. Ha, T.D. Minh, H.M. Nguyet, A.K. Sharma, Ampicillin adsorption onto amine-functionalized magnetic graphene oxide: synthesis, characterization and removal mechanism, Kor. J. Chem. Eng. 38 (1) (2021) 22–31.
- [35] Q. Yang, X. Wang, W. Luo, J. Sun, Q. Xu, F. Chen, J. Zhao, S. Wang, F. Yao, D. Wang, X. Li, G. Zeng, Effectiveness and mechanisms of phosphate adsorption on iron-modified biochar derived from waste activated sludge, Biore sour. Technol. 247 (2018) 537–544.
- [36] G.-J. Jiao, J. Ma, Y. Zhang, D. Jin, Y. Li, C. Hu, Y. Guo, Z. Wang, J. Zhou, R. Sun, Nitrogen-doped lignin-derived biochar with enriched loading of CeO₂ nanoparticles for highly efficient and rapid phosphate capture, Int. J. Biol. Macromol. 182 (2021) 1484–1494.
- [37] G. Eka Putri, Y. Rilda, S. Syukri, A. Labanni, S. Arief, Highly antimicrobial activity of cerium oxide nanoparticles synthesized using *Moringa oleifera* leaf extract by a rapid green precipitation method, J. Mater. Res. Technol. 15 (2021) 2355–2364.
- [38] Y. Xiong, S. Chen, F. Ye, L. Su, C. Zhang, S. Shen, S. Zhao, Synthesis of a mixed valence state Ce-MOF as an oxidase mimetic for the colorimetric detection of biothiols, Chem. Commun. 51 (22) (2015) 4635–4638.
- [39] A.A. Ansari, A. Kaushik, Synthesis and optical properties of nanostructured Ce(OH)₄, J. Semiconduct. 31 (3) (2010), 033001.
- [40] S. Zhang, X. Yang, M. Ju, L. Liu, K. Zheng, Mercury adsorption to aged biochar and its management in China, Environ. Sci. Pollut. Res. (2018).
- [41] S.F. Jiang, K.F. Xi, J. Yang, H. Jiang, Biochar-supported magnetic noble metallic nanoparticles for the fast recovery of excessive reductant during pollutant reduction, Chemosphere 227 (2019) 63–71.

- [42] P. Manasa, Z.J. Lei, F. Ran, Biomass waste derived low cost activated carbon from *carchorus olitorius* (Jute Fiber) as sustainable and novel electrode material, *J. Energy Storage* 30 (2020) 101494.
- [43] A. Hai, G. Bharath, K.R. Babu, H. Taher, M. Naushad, F. Banat, Date seeds biomass-derived activated carbon for efficient removal of NaCl from saline solution, *Process Saf. Environ. Protect.* 129 (2019) 103–111.
- [44] A.I. Argüelles-Pesqueira, N.M. Diéguez-Armenta, A.K. Bobadilla-Valencia, S.K. Nataraj, A. Rosas-Durazo, R. Esquivel, M.E. Alvarez-Ramos, R. Escudero, P. Guerrero-German, J.A. Lucero-Acuña, P. Zavala-Rivera, Low intensity sonosynthesis of iron carbide@iron oxide core-shell nanoparticles, *Ultrason. Sonochem.* 49 (2018) 303–309.
- [45] P.J. Mafa, B.B. Mamba, A.T. Kuvaraga, Photoelectrocatalytic evaluation of EG-CeO₂ photoanode on degradation of 2,4-dichlorophenol, *Sol. Energy Mater. Sol. Cells* 208 (2020) 110416.
- [46] C. Ding, W. Cheng, Y. Sun, X. Wang, Novel fungus-Fe₃O₄ bio-nanocomposites as high-performance adsorbents for the removal of radionuclides, *J. Hazard Mater.* 295 (2015) 127–137.
- [47] N. Wang, Y. Qiu, T. Xiao, J. Wang, Y. Chen, X. Xu, Z. Kang, L. Fan, H. Yu, Comparative studies on Pb(II) biosorption with three spongy microbe-based biosorbents: high performance, selectivity and application, *J. Hazard Mater.* (2019).
- [48] Y. Su, Y. Wen, W. Yang, X. Zhang, M. Xia, N. Zhou, Y. Xiong, Z. Zhou, The mechanism transformation of ramie biochar's cadmium adsorption by aging, *Bioresour. Technol.* 330 (2021) 124947.
- [49] N. Kasera, S. Hall, P. Kolar, Effect of surface modification by nitrogen-containing chemicals on morphology and surface characteristics of N-doped pine bark biochars, *J. Environ. Chem. Eng.* 9 (2) (2021) 105161.
- [50] J. Alchouron, C. Navarathna, H.D. Chludil, N.B. Dewage, F. Perez, E.B. Hassan, C.U. Pittman Jr., A.S. Vega, T.E. Mlsna, Assessing South American Guadua chacoensis bamboo biochar and Fe₃O₄ nanoparticle dispersed analogues for aqueous arsenic(V) remediation, *Sci. Total Environ.* 706 (2020) 135943.
- [51] F.L. Rivera, F.J. Recio, F.J. Palomares, J. Sánchez-Marcos, N. Menéndez, E. Mazarío, P. Herrasti, Fenton-like degradation enhancement of methylene blue dye with magnetic heating induction, *J. Hem.* 879 (2020) 114773.
- [52] G. Yin, X. Song, L. Tao, B. Sarkar, A.K. Sarmah, W. Zhang, Q. Lin, R. Xiao, Q. Liu, H. Wang, Novel Fe-Mn binary oxide-biochar as an adsorbent for removing Cd(II) from aqueous solutions, *Chem. Eng. J.* 389 (2020) 124465.
- [53] K. Xiao, F. Liang, J. Liang, W. Xu, Z. Liu, B. Chen, X. Jiang, X. Wu, J. Xu, J. Beiyuan, H. Wang, Magnetic bimetallic Fe, Ce-embedded N-enriched porous biochar for peroxymonosulfate activation in metronidazole degradation: applications, mechanism insight and toxicity evaluation, *Chem. Eng. J.* 433 (2022) 134387.
- [54] E. Paparazzo, On the number, binding energies, and mutual intensities of Ce3d peaks in the XPS analysis of cerium oxide systems: a response to Murugan et al. Superlattice. *Microst.* 85 (2017) 321 (2015) Superlattices and Microst. 105, 216–220.
- [55] Y. Song, P. Yuan, P. Du, L. Deng, Y. Wei, D. Liu, X. Zhong, J. Zhou, A novel halloysite-CeO_x nanohybrid for efficient arsenic removal, *Appl. Clay Sci.* 186 (2020) 105450.
- [56] Z. Chen, Y. Xie, K. Li, L. Huang, X. Zheng, Synthesis of carbon coated-ceria with improved cytocompatibility, *Ceram. Int.* 45 (16) (2019) 19981–19990.
- [57] G. Yu, F. Fu, Exploration of different adsorption performance and mechanisms of core-shell Fe₃O₄@Ce-Zr oxide composites for Cr(VI) and Sb(III), *J. Colloid Interface Sci.* 576 (2020) 10–20.
- [58] L. Cui, J. Cui, H. Zheng, Y. Wang, Y. Qin, X. Shu, J. Liu, Y. Zhang, Y. Wu, Construction of NiO/MnO₂/CeO₂ hybrid nanoflake arrays as platform for electrochemical energy storage, *J. Power Sources* 361 (2017) 310–317.
- [59] C.D. Dong, C.W. Chen, T.B. Nguyen, C.P. Huang, C.M. Hung, Degradation of phthalate esters in marine sediments by persulfate over Fe-Ce/biochar composites, *Chem. Eng. J.* 384 (2020) 123301.
- [60] X. Peng, Y. Deng, L. Liu, X. Tian, S. Gang, Z. Wei, X. Zhang, K. Yue, The addition of biochar as a fertilizer supplement for the attenuation of potentially toxic elements in phosphogypsum-amended soil, *J. Clean. Prod.* 277 (2020) 124052.
- [61] Y.K. Choi, T.R. Choi, R. Gurav, S.K. Bhatia, Y.L. Park, H.J. Kim, E. Kan, Y.H. Yang, Adsorption behavior of tetracycline onto *Spirulina* sp. (microalgae)-derived biochars produced at different temperatures, *Sci. Total Environ.* 710 (2020) 136282.
- [62] S. Lagergren, Zur theorie der Sogenannten adsorption Gelöster stoffe, *Kungliga Svenska Vetenskapsakademiens* 24 (1898) 1–39.
- [63] Y. Ho, Review of second-order models for adsorption systems, *J. Hazard Mater.* 136 (3) (2006) 681–689.
- [64] C. Aharoni, F.C. Tompkins, Kinetics of adsorption and desorption and the Elovich equation, in: D.D. Eley, H. Pines, P.B. Weisz (Eds.), *Adv. Catal.* 21 (1970) 1–49.
- [65] M. De la Luz-Asunción, E.E. Pérez-Ramírez, A.L. Martínez-Hernández, P.E. García-Casillas, J.G. Luna-Bárcenas, C. Velasco-Santos, Adsorption and kinetic study of Reactive Red 2 dye onto graphene oxides and graphene quantum dots, *Diam. Relat. Mater.* 109 (2020) 108002.
- [66] E. Salehi, M. Askari, M. Velashjerdi, B. Arab, Phosphoric acid-treated spent tea residue biochar for wastewater decoloring: batch Adsorption study and process intensification using multivariate data-based optimization, *Chem. Eng. Process* 158 (2020) 108170.
- [67] J. Heo, Y. Yoon, G. Lee, Y. Kim, J. Han, C.M. Park, Enhanced adsorption of bisphenol A and sulfamethoxazole by a novel magnetic CuZnFe₂O₄-biochar composite, *Bioresour. Technol.* 281 (2019) 179–187.
- [68] N.A. Elessawy, M.H. Gouda, S. M. Ali, M. Salerno, M.S.M. Eldin, Effective elimination of contaminant antibiotics using high-surface-area magnetic-functionalized graphene nanocomposites developed from plastic waste, *Mater.* 13 (7) (2020) 1517.
- [69] A. Onder, P. Ilgin, H. Ozay, O. Ozay, Removal of dye from aqueous medium with pH-sensitive poly [(2-(acryloyloxy) ethyl] trimethyl ammonium chloride-co-1-vinyl-2-pyrrolidone] cationic hydrogel, *J. Environ. Chem. Eng.* 8 (5) (2020) 104436.
- [70] G. Bayramoglu, A. Akbulut, G. Liman, M.Y. Arica, Removal of metal complexed azo dyes from aqueous solution using tris(2-aminoethyl) amine ligand modified magnetic p(GMA-EGDMA) cationic resin: adsorption, isotherm and kinetic studies, *Chem. Eng. Res. Des.* 124 (2017) 85–97.
- [71] M.I. Temkin, V. Pyzhev, Kinetic of ammonia synthesis on promoted iron catalyst, *Acta Phys. Chem. URSS* 12 (1940) 327–356.
- [72] Y. Cantu, A. Remes, A. Reyna, D. Martinez, J. Villarreal, H. Ramos, S. Trevino, C. Tamez, A. Martinez, T. Eubanks, J.G. Parsons, Thermodynamics, Kinetics, and Activation energy Studies of the sorption of chromium (III) and chromium (VI) to a Mn₃O₄ nanomaterial, *Chem. Eng. Sci.* 254 (2014) 374–383.
- [73] H.K. Bopari, M. Joseph, D.M. O'Carroll, Kinetics and thermodynamics of cadmium ion removal by adsorption onto nano zerovalent iron particles, *J. Hazard Mater.* 186 (1) (2011) 458–465.
- [74] J. Imanipoor, A. Ghafelebashi, M. Mohammadi, M. Dinari, M.R. Ehsani, Fast and effective adsorption of amoxicillin from aqueous solutions by L-methionine modified montmorillonite K10, *Colloids Surf. A Physicochem. Eng. Asp.* 611 (2021) 125792.
- [75] Y. Gao, D. He, L. Wu, Z. Wang, Y. Yao, Z.-H. Huang, H. Yang, M.-X. Wang, Porous and ultrafine nitrogen-doped carbon nanofibers from bacterial cellulose with superior adsorption capacity for adsorption removal of low-concentration 4-chlorophenol, *Chem. Eng. J.* 127411 (2020).
- [76] A. Boukhelkhal, O. Benkortbi, M. Hamadache, Use of an anionic surfactant for the sorption of a binary mixture of antibiotics from aqueous solutions, *Environ. Technol.* 40 (25) (2019) 3328–3336.
- [77] V.S. Munagapati, D.S. Kim, Equilibrium isotherms, kinetics, and thermodynamics studies for Congo red adsorption using calcium alginate beads impregnated with nano-goethite, *Ecotoxicol. Environ. Saf.* 141 (2017) 226–234.
- [78] O.P. Bansal, Thermodynamics of equilibrium adsorption of antibiotics by clay minerals and humic acid-clay complexes, *Natl. Acad. Sci. Lett.* 35 (2) (2012) 109–114.
- [79] A.K. Rahardjo, M.J.J. Susanto, A. Kurniawan, N. Indraswati, S. Ismadji, Modified Ponorogo bentonite for the removal of ampicillin from wastewater, *J. Hazard Mater.* 190 (1–3) (2011) 1001–1008.
- [80] Z. Qi, T.P. Joshi, R. Liu, H. Liu, J. Qu, Synthesis of Ce(III)-doped Fe₃O₄ magnetic particles for efficient removal of antimony from aqueous solution, *J. Hazard Mater.* 329 (2017) 193–204.
- [81] T. Hertel, J. Neubauer, F. Goetz-Neunhoeffer, Study of hydration potential and kinetics of the ferrite phase in iron-rich CAC, *Cement Concr. Res.* 83 (2016) 79–85.
- [82] Y. Cao, X. Xie, X. Tong, D. Feng, J. Lv, Y. Chen, Q. Song, The activation mechanism of Fe(II) ion-modified cassiterite surface to promote salicylhydroxamic acid adsorption, *Miner. Eng.* 160 (2021) 106707.
- [83] F. Wang, H. Sun, X. Ren, K. Zhang, Sorption of naphthalene and its hydroxyl substitutes onto biochars in single-solute and bi-solute systems with propranolol as the co-solute, *Chem. Eng. J.* 326 (2017) 281–291.
- [84] R. Chitongo, B.O. Opeolu, O.S. Olatunji, Abatement of Amoxicillin, Ampicillin, and Chloramphenicol from aqueous solutions using activated carbon prepared from grape slurry, *Clean* 47 (2) (2019) 1800077.
- [85] V. Nairi, L. Medda, M. Monduzzi, A. Salis, Adsorption and release of ampicillin antibiotic from ordered mesoporous silica, *J. Colloid Interface Sci.* 497 (2017) 217–225.
- [86] D. Balarak, F. Mostafapour, H. Azarpira, A. Joghataei, Langmuir, Freundlich, Temkin and Dubinin–Radushkevich isotherms studies of equilibrium sorption of ampicillin unto montmorillonite nanoparticles, *J. Pharm. Res. Int.* 20 (2017) 1–9.
- [87] N. Rahman, P. Varshney, Assessment of Ampicillin removal efficiency from aqueous solution by polydopamine/zirconium (IV) iodate: optimization by response surface methodology, *RSC Adv.* 10 (34) (2020) 20322–20337.